Acta Mechanica Sinica (2019) 35(4):879–893
https://doi.org/10.1007/s10409-019-00851-4

RESEARCH PAPER

Free vibration analysis of a spinning piezoelectric beam with geometric nonlinearities

Wei Li[1] · Xiao-Dong Yang[1] · Wei Zhang[1] · Yuan Ren[2] · Tian-Zhi Yang[3]

Received: 23 October 2018 / Revised: 19 December 2018 / Accepted: 3 January 2019 / Published online: 13 May 2019

Abstract
The linear and non-linear free vibrations of a spinning piezoelectric beam are studied by considering geometric nonlinearities and electromechanical coupling effect. The non-linear differential equations of the spinning piezoelectric beam governing two transverse vibrations are derived by using transformation of two Euler angles and the extended Hamilton principle, wherein an additional piezoelectric coupling term and different linear terms are present in contrast to the traditional shaft model. Linear frequencies are obtained by solving the standard eigenvalues of the linearized system directly, and the non-linear frequencies and non-linear complex modes are achieved by using the method of multiple scales. For free vibrations analysis of a spinning piezoelectric beam, the non-linear modal motions are investigated as forward and backward precession with different spinning speeds. The responses to the initial conditions for this gyroscopic system are studied and a beat phenomenon is found, which are then validated by numerical simulation. The influences of some parameters such as electrical resistance, rotary inertia and spinning speeds to the non-linear dynamics of a spinning piezoelectric beam are investigated.

Keywords Spinning piezoelectric beam · Free vibrations · Non-linear frequencies · Complex modes

1 Introduction

A spinning piezoelectric beam can often be used to make a piezoelectric vibratory gyroscope, which has several applications such as in mobile phones, high-grade cars, intelligent robotics, military weapons and aerospace systems. In the past, the piezoelectric vibratory gyroscope has become one of the best essential electromechanical system sensors, especially in the field of inertial navigation systems [1]. To simplify the analysis of the piezoelectric gyroscope, traditionally, most investigations are confined to the linear system with piezoelectric excitation and piezoelectric detection [2, 3]. Based on the linear approximation and non-linear "slow" system, Lajimi et al. [4] investigated the non-linear estimate of the mechanical thermal noise for an electrostatic gyroscope. The applications of non-linear analysis are also significant for flexible components, and the characteristics of the non-linear gyroscopic system have attracted much attention in a field of rotating shaft [5, 6]. By using the fractional calculus and the Gurtin–Murdoch theory, Oskouie et al. [7] investigated the nonlinear vibration of viscoelastic Euler–Bernoulli nanobeam. By considering three types of boundary conditions, Zhao et al. [8] studied the natural frequencies of the Timoshenko beam with surface effects. Recently, there has been a growing research interest to investigate piezoelectric materials on energy harvesters [9–11] and microstructures [12–15] for rotational motion. As a conclusion, the non-linear characteristics of gyroscopes modeled by a spinning piezoelectric beam should be investigated, so that the guidance to improve the performance of piezoelectric vibratory gyroscope can be proposed.

Modal analysis of gyroscopic system is an effective tool to investigate the dynamic responses and mode interactions [16, 17]. However, when coping with the gyroscopic continuum, the modal theories become difficult because the complex modes should be considered [18, 19]. To this end, Rosenburg [20] firstly presented the non-linear normal modes, which expanded the modal motions from the linear non-gyroscopic systems to non-linear non-gyroscopic systems. The non-linear

✉ Xiao-Dong Yang
jxdyang@163.com

1 Beijing Key Laboratory of Non-linear Vibrations and Strength of Mechanical Engineering, College of Mechanical Engineering, Beijing University of Technology, Beijing 100124, China

2 Department of Aerospace Science and Technology, Space Engineering University, Beijing 101416, China

3 Department of Mechanics, Tianjin University, Tianjin 300072, China

normal mode concept is utilized in the field of non-linear systems by many researchers. By using the multiple scales method, Nayfeh and Nayfeh [21, 22] studied the non-linear normal modes with internal resonance and geometric non-linearity of a one-dimensional continuous system. To solve the modal motions of gyroscopic systems, Shaw and Pierre [23, 24] used the invariant manifold method to expand the non-linear normal modes to the gyroscope coupling systems. The work of Carlos et al. [25] made a comparison for the non-linear normal modes of an axially loaded beam by both the invariant manifold method and multiple scales method. For a linear system, Uspensky and Avramov [26] studied the non-linear normal mode under a forced excitation by using the invariant manifold method and Rauscher method. To analyze the free vibration of a gyroscopic system, Arvin and Nejad [27] described the complex dynamical characteristics of non-linear normal modes. In their work, Qian et al. [28] studied parametric instability analysis of a linear gyroscopic system based on the traditional coupled gyroscopic system and decoupled gyroscopic modes decoupling method. Recently, there are several valuable research towards non-linear normal modes of undamped systems [29–31] and damped systems [32, 33] by using numerical calculation. The study by Pan et al. [34] used the complex modal technique to evaluate the natural frequencies and complex modes of serpentine belt drives.

The gyroscopic effect caused by spinning motion appears comprehensively in the rotor dynamics systems [35, 36]. By deriving the closed polynomial of frequency equations and integral forms under an ordinary forcing function, Sturla and Argento [37] studied the free and forced vibrations of a viscoelastic rotating Rayleigh beam. The work Ishida and Inoue [38] considered the effect of internal resonance of a non-linear rotor. It is always hard to gain the physical model of nonlinear rotor-bearing system, thus Ma et al. [39] identified a data-driven non-linear auto-regressive network with exogenous inputs (NARX) model to solve this problem. By considering random excitations, Hosseini and Khadem [40] investigated the vibration and stability of a spinning beam with random characteristics subject to white noise by using the finite element method. In order to guide the design of distorted model, Luo et al. [41] provided a new dynamic scaling law of geometrically distorted model in predicting the dynamic characteristics. Moreover, many researchers analyzed the free vibrations dynamic properties of shafts by different methods [5, 6, 42, 43].

In this paper, the piezoelectric coupling governing differential expressions with non-linearities in curvature and inertia of a spinning piezoelectric beam are obtained, and the natural frequencies, as well as gyroscopic complex modes, are analyzed. By using the multiple scales method, the non-linear modal motions and non-linear frequencies are investigated. The responses to the initial values are discussed for the gyroscopic system by multiple scales method, and numerical simulation validates the results. The piezoelectric coupling effect and non-linear features of the gyroscopic continuum are also investigated in detail. The contribution of the electrical resistance, rotary inertia, electromechanical coupling coefficient and spinning speeds to the forward and backward natural frequencies of the spinning piezoelectric beam are studied, which prompts possible optimizations in the design of piezoelectric vibratory gyroscopes.

2 Governing equations of a spinning piezoelectric beam

Figure 1 shows the structure of a spinning beam which is surrounded with four piezoelectric films. The length (L_1, L_2, L) and width (w_b, w_p) of the beam and piezoelectric films are shown in the figure. The beam displacement is made of three

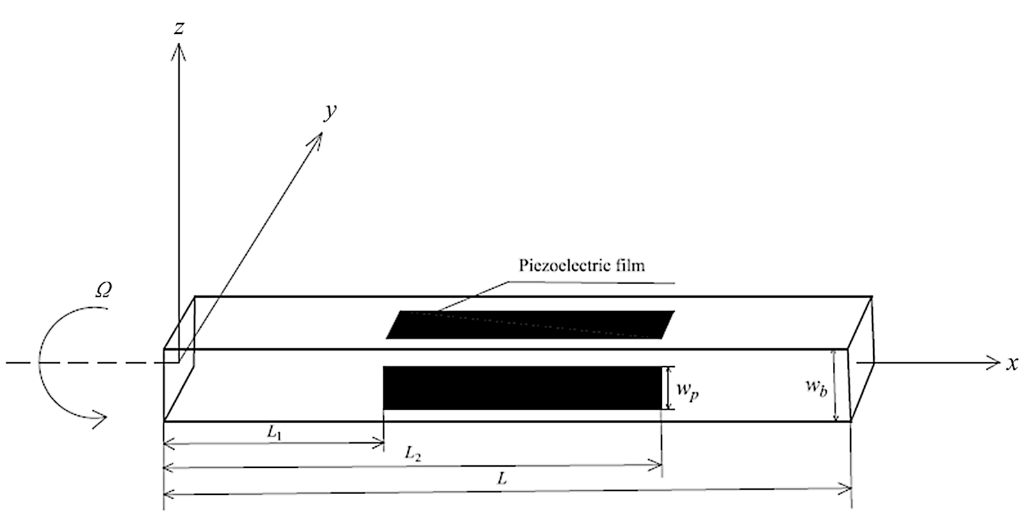

Fig. 1 Spinning beam with surrounded four piezoelectric films

components, $u(s, t)$, $v(s, t)$, and $w(s, t)$, along the inertial frame x, y, and z directions, respectively, where s denotes the undeformed arclength along the x-axis from the root of the beam to the observed reference point, t denotes time. The x–y–z coordinate system denotes the inertial frame.

The transformation of two Euler angles by which an arbitrary beam cross section can be expressed with three coordinate systems is shown in Fig. 2. The x_0–y_0–z_0 system is a spinning frame around the x-axis with constant speed Ω of the undeformed beam; the x_1–y_1–z_1 and x_2–y_2–z_2 systems are orthogonal coordinate frames associated with Euler angle transformation. Moreover, we let $(\boldsymbol{i}_x, \boldsymbol{i}_y, \boldsymbol{i}_z)$, $(\boldsymbol{i}_{\hat{1}}, \boldsymbol{i}_{\hat{2}}, \boldsymbol{i}_{\hat{3}})$, and $(\boldsymbol{i}_1, \boldsymbol{i}_2, \boldsymbol{i}_3)$ represent the unit vectors of the x_0–y_0–z_0, x_1–y_1–z_1, and x_2–y_2–z_2 coordinate frames, respectively.

From the undeformed plane, the cross section first spins by α degree about n axis from x_0–y_0–z_0 to x_1–y_1–z_1

$$\begin{Bmatrix} \boldsymbol{i}_{\hat{1}} \\ \boldsymbol{i}_{\hat{2}} \\ \boldsymbol{i}_{\hat{3}} \end{Bmatrix} = \boldsymbol{B}(\alpha) \begin{Bmatrix} \boldsymbol{i}_x \\ \boldsymbol{i}_y \\ \boldsymbol{i}_z \end{Bmatrix}. \tag{1}$$

The transformation matrix $\boldsymbol{B}(\alpha)$ can be expressed by the displacements [44]

$$\boldsymbol{B}(\alpha) = \begin{bmatrix} 1+u' & v' & w' \\ -v' & 1+u'+\frac{w'^2}{2+u'} & -\frac{v'w'}{2+u'} \\ -w' & -\frac{v'w'}{2+u'} & 1+u'+\frac{v'^2}{2+u'} \end{bmatrix}. \tag{2}$$

Here, the primes of (u, v, w) denote the derivatives with respect to s, respectively.

Further, the cross-section spins ϕ by about x_1 axis from x_1–y_1–z_1 to x_2–y_2–z_2, thus the transformation from x_0–y_0–z_0 to x_2–y_2–z_2 is

$$\begin{Bmatrix} \boldsymbol{i}_1 \\ \boldsymbol{i}_2 \\ \boldsymbol{i}_3 \end{Bmatrix} = \boldsymbol{P} \begin{Bmatrix} \boldsymbol{i}_x \\ \boldsymbol{i}_y \\ \boldsymbol{i}_z \end{Bmatrix}, \quad \boldsymbol{P} = \begin{bmatrix} 1 & 0 & 0 \\ 0 & \cos\phi & \sin\phi \\ 0 & -\sin\phi & \cos\phi \end{bmatrix} \boldsymbol{B}(\alpha). \tag{3}$$

For an in-extensional beam, $u' \cong -(v'^2 + w'^2)/2$, expanding ϕ with a Taylor series, $\cos\phi = 1 - \phi^2/2$, $\sin\phi = \phi - \phi^3/6$, the transformation matrix $\boldsymbol{P}$ can be attained as

$$\boldsymbol{P} = \begin{bmatrix} 1 - \frac{1}{2}v'^2 - \frac{1}{2}w'^2 & v' & w' \\ -v' - w'\phi + \frac{1}{2}v'\phi^2 & 1 - \frac{1}{2}v'^2 - \frac{1}{2}\phi^2 - \frac{1}{2}\phi v'w' & \phi - \frac{1}{2}v'w' - \frac{1}{2}w'^2\phi - \frac{1}{6}\phi^3 \\ -w' + v'\phi + \frac{1}{2}w'\phi^2 & -\phi - \frac{1}{2}v'w' + \frac{1}{2}v'^2\phi + \frac{1}{6}\phi^3 & 1 - \frac{1}{2}w'^2 - \frac{1}{2}\phi^2 + \frac{1}{2}v'w'\phi \end{bmatrix}. \tag{4}$$

Using the concept of continuity, one can obtain the deformed curvatures ρ_i $(i = 1, 2, 3)$

$$\begin{aligned} \rho_1 &\equiv \boldsymbol{i}_2' \cdot \boldsymbol{i}_3 = \sum_{i=1}^{3} P_{2i}' P_{3i} = \phi' + \frac{1}{2}v''w' - \frac{1}{2}v'w'', \\ \rho_2 &\equiv -\boldsymbol{i}_1' \cdot \boldsymbol{i}_3 = -\sum_{i=1}^{3} P_{1i}' P_{3i} = -w'' + v''\phi \\ &\quad - \frac{1}{2}v'v''w' - \frac{1}{2}w''w'^2 + \frac{1}{2}\phi^2 w'', \\ \rho_3 &\equiv \boldsymbol{i}_1' \cdot \boldsymbol{i}_2 = \sum_{i=1}^{3} P_{1i}' P_{2i} = v'' + w''\phi \\ &\quad + \frac{1}{2}v''v'^2 + \frac{1}{2}v'w'w'' - \frac{1}{2}\phi^2 v''. \end{aligned} \tag{5}$$

The relative angular velocity vector $\boldsymbol{\omega}$ to the inertial frame are then obtained as

$$\begin{aligned} \omega_1 &\equiv \dot{\boldsymbol{i}}_2 \cdot \boldsymbol{i}_3 = \sum_{i=1}^{3} (\dot{P}_{2i} P_{3i} + \Omega P_{1i}) = \Omega + \dot{\phi} \\ &\quad + \frac{1}{2}\dot{v}'w' - \frac{1}{2}v'\dot{w}' - \frac{1}{2}\Omega v'^2 - \frac{1}{2}\Omega w'^2, \\ \omega_2 &\equiv -\dot{\boldsymbol{i}}_1 \cdot \boldsymbol{i}_3 = -\sum_{i=1}^{3} \dot{P}_{1i} P_{3i} = -\Omega v' - \Omega w'\phi + \dot{v}'\phi - \dot{w}', \\ \omega_3 &\equiv \dot{\boldsymbol{i}}_1 \cdot \boldsymbol{i}_2 = \sum_{i=1}^{3} \dot{P}_{1i} P_{2i} = -\Omega w' + \Omega v'\phi + \dot{w}'\phi + \dot{v}'. \end{aligned} \tag{6}$$

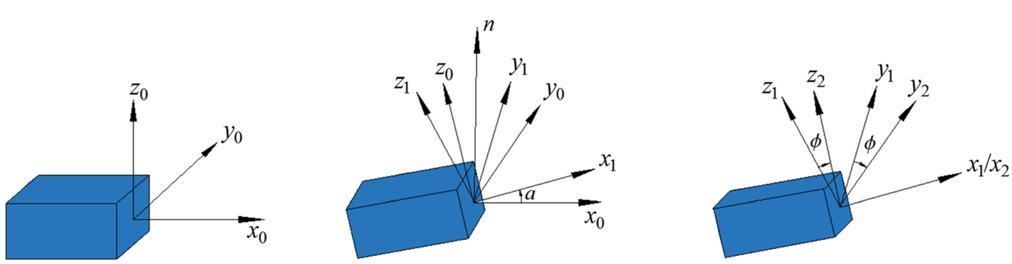

Fig. 2 Sequence of Euler angle transformation

Here, the dots of (u, v, w) denote the derivatives with respect to t, respectively.

The deformation of any point on the beam can be denoted by the position vector $\boldsymbol{R}$ as

$$\boldsymbol{R} = u\boldsymbol{i}_x + v\boldsymbol{i}_y + w\boldsymbol{i}_z + y\boldsymbol{i}_2 + z\boldsymbol{i}_3. \tag{7}$$

Using directional time derivatives, $\dot{\boldsymbol{R}}$ in the coordinate system of x_0–y_0–z_0 is expressed as

$$\dot{\boldsymbol{R}} = \dot{u}\boldsymbol{i}_x + (\dot{v} - w\Omega)\boldsymbol{i}_y + (\dot{w} + v\Omega)\boldsymbol{i}_z + \left(\boldsymbol{i}_x \ \boldsymbol{i}_y \ \boldsymbol{i}_z\right)\boldsymbol{P}^{\mathrm{T}}\boldsymbol{r}\boldsymbol{\omega}, \tag{8}$$

with

$$\boldsymbol{r} = \begin{bmatrix} 0 & z & -y \\ -z & 0 & 0 \\ y & 0 & 0 \end{bmatrix}, \ \boldsymbol{\omega} = \begin{Bmatrix} \omega_1 \\ \omega_2 \\ \omega_3 \end{Bmatrix}. \tag{9}$$

The kinetic energy of a spinning Rayleigh beam can be obtained by substituting Eqs. (6), (8), and (9) into the following expression

$$T = \frac{1}{2}\int_0^L \int_A \rho\dot{\boldsymbol{R}} \cdot \dot{\boldsymbol{R}}\mathrm{d}A\mathrm{d}s. \tag{10}$$

According to the assumption of an inextensional beam and using the geometric boundary condition $u(0,t) = 0$, one can obtain

$$u = -\frac{1}{2}\int_0^s \left(w'^2 + v'^2\right)\mathrm{d}s. \tag{11}$$

Hence, the kinetic energy can be obtained as

$$\begin{aligned} T = &\frac{1}{2}\int_0^L \left\{ m\left\{ \dot{w}^2 + \dot{v}^2 + \left[-\frac{1}{2}\int_0^s \frac{\partial}{\partial t}\left(w'^2 + v'^2\right)\mathrm{d}s\right]^2 \right\}\right. \\ &\left. + m\Omega^2\left(w^2 + v^2\right) + 2m\Omega(v\dot{w} - w\dot{v})\right\}\mathrm{d}s \\ &+ \frac{1}{2}\int_0^L \left[j\left(\dot{v}'^2 + \dot{w}'^2\right) + j\Omega^2\left(v'^2 + w'^2\right)\right. \\ &\left. + 2j\Omega\left(v'\dot{w}' + w'\dot{v}'\right)\right]\mathrm{d}s + jL\Omega^2, \end{aligned} \tag{12}$$

with

$$\begin{aligned} &m = w_b\rho_b h_b + 4S(s)w_p\rho_p h_p, \quad j = \int_A \rho(s)z^2\mathrm{d}A = \int_A \rho(s)y^2\mathrm{d}A, \\ &\rho(s) = \rho_b + S(s)\rho_p, \quad S(s) = H(s - L_1) - H(s - L_2). \end{aligned} \tag{13}$$

In Eq. (13), $H(s)$ is the Heaviside function, A is the cross-sectional area of the beam, m, $\rho(s)$, and j are the total mass, total density, and total rotary inertia of the beam and the piezoelectric films, respectively, and $\rho_{b,p}$, $w_{b,p}$, and $h_{b,p}$ ($w_b/h_b = 1$) are the volumetric mass density, width and thickness of the beam and the piezoelectric film, respectively. For all the parameters used in this paper, subscript b denotes the beam material and p denotes piezoelectric film.

The mechanical properties of piezoelectric films are coupled with their electric properties. For the configuration and non-linear strain considered here, the electrical displacement is one dimensional and the stress–strain relations for these materials are known as follows [45, 46]

$$\begin{aligned} &T_p = E_p S - e_{31}E_3, \quad D = e_{31}S + \varepsilon_{33}E_3, \\ &S = -y\rho_3 + z\rho_2, \quad E_3 = \frac{V_{v,w}}{h}, \end{aligned} \tag{14}$$

where E_p is the stiffness coefficient, ε_{33} is the dielectric permittivity, T_p is the stress, S is the strain, e_{31} is the piezoelectric strain constant, D is the electrical displacement, E_3 is the electrical field, and $V_{v,w}$ is the voltage. The relation between voltage and current is

$$V_w = Z\dot{Q}_w, V_v = Z\dot{Q}_v, \tag{15}$$

where Z is electrical resistance, Q is charge quantity.

An isotropic beam is considered, and the stress–strain satisfies the relation

$$T_b = E_b S, \tag{16}$$

where E_b stands for stiffness coefficient.

The total potential energy for spinning beam can be derived as follows

$$U = \frac{1}{2}\int_{V_b} T_b S\mathrm{d}V_b + \frac{1}{2}\int_{V_p} (T_p S - DE_3)\mathrm{d}V_p. \tag{17}$$

Substituting Eq. (15) into Eq. (14), then further inserting the results and Eq. (16) into Eq. (17), we can obtain

$$\begin{aligned} U = &\frac{EI}{2}\int_0^L \left(\rho_2^2 + \rho_3^2\right)\mathrm{d}s + \frac{\theta}{2}\int_{L_1}^{L_2} (-\rho_2 Z\dot{Q}_w + \rho_3 Z\dot{Q}_v)\mathrm{d}s \\ &- \frac{C_p}{2}\int_{L_1}^{L_2} \left[(Z\dot{Q}_w)^2 + (Z\dot{Q}_v)^2\right]\mathrm{d}s, \end{aligned} \tag{18}$$

where $EI = E_b I_b + S(s)E_p I_p$ is bending stiffness, $C_p = w_p\varepsilon_{33}/h_p$ is piezoelectric film capacitor, $\theta = w_p e_{31}(h_b/2 + h_p)$ is electromechanical coupling coefficient, and

$$I_b = \frac{1}{12}w_b h_b^3, \quad I_p = 2\left[\frac{1}{12}w_p h_p^3 + w_p h_p\left(\frac{h_p}{2} + \frac{h_b}{2}\right)^2 + \frac{1}{12}h_p w_p^3\right]. \tag{19}$$

The virtual work done by mechanical damping and electrical resistance is

$$\delta W = -\frac{1}{2}\int_0^L (c\dot{v}\delta v + c\dot{w}\delta w + Z\dot{Q}_w\delta Q_w + Z\dot{Q}_v\delta Q_v)\mathrm{d}s. \tag{20}$$

The next step is to substitute the results of kinetic, potential energy and virtual work into the Hamilton principle

$$\int_{t_1}^{t_2} (\delta T - \delta U + \delta W)\mathrm{d}t = 0. \tag{21}$$

Because the torsional frequency is larger than the flexural frequency, so the twist angle ϕ can be neglected [42]. By using voltage and current relation and expanding the results up to three orders, we can obtain the following four partial governing equations with electromechanical coupling

$$\begin{aligned}
&m(\ddot{v} - \dot{\Omega}w - 2\Omega\dot{w} - \Omega^2 v) - j(\Omega^2 v'' + \ddot{v}'') \\
&\quad + EI[v'(v'v'' + w'w'')' + v''']' + c\dot{v} \\
&\quad + \frac{1}{2}\left\{ v' \int_L^s \frac{\partial^2}{\partial t^2}\left[\int_0^s (v'^2 + w'^2)\mathrm{d}s\right]\mathrm{d}s \right\}' \\
&\quad - \theta V_v(t) S(s)'' = 0, \\
&m(\ddot{w} + \dot{\Omega}v + 2\Omega\dot{v} - \Omega^2 w) - j(\Omega^2 w'' + \ddot{w}'') \\
&\quad + EI[w'(v'v'' + w'w'')' + w''']' + c\dot{w} \\
&\quad + \frac{1}{2}\left\{ w' \int_L^s \frac{\partial^2}{\partial t^2}\left[\int_0^s (v'^2 + w'^2)\mathrm{d}s\right]\mathrm{d}s \right\}' \\
&\quad - \theta V_w(t) S(s)'' = 0, \\
&C_p \dot{V}_v(t) + \frac{V_v(t)}{Z} + \theta S(s)'' \dot{v} = 0, \\
&C_p \dot{V}_w(t) + \frac{V_w(t)}{Z} + \theta S(s)'' \dot{w} = 0.
\end{aligned} \tag{22}$$

Substituting periodic voltages $\{v, w, V_v, V_w\} = \{\bar{v}, \bar{w}, \bar{V}_v, \bar{V}_w\}\mathrm{e}^{\mathrm{i}\omega t}$ into the last two equations of Eq. (22), removing the overbar above the displacements and voltages for simplification, we obtain

$$\begin{aligned}
&\left(1 + \frac{Z_0}{Z}\right)V_v + \frac{\theta}{C_p} S(s)'' v = 0, \\
&\left(1 + \frac{Z_0}{Z}\right)V_w + \frac{\theta}{C_p} S(s)'' w = 0,
\end{aligned} \tag{23}$$

with $Z_0 = 1/(\mathrm{i}\omega C_p)$.

Hence, substituting Eq. (23) into Eq. (22), the last two equations of (22) can be eliminated by using displacements to replace voltages [47], and then the equations can be reduced to partial differential equations of two degrees of freedom

$$\begin{aligned}
&m(\ddot{v} - \dot{\Omega}w - 2\Omega\dot{w} - \Omega^2 v) - j(\Omega^2 v'' + \ddot{v}'') \\
&\quad + EI[v'(v'v'' + w'w'')' + v''']' + c\dot{v} \\
&\quad + \frac{1}{2}m\left\{ v' \int_L^s \frac{\partial^2}{\partial t^2}\left[\int_0^s (v'^2 + w'^2)\mathrm{d}s\right]\mathrm{d}s \right\}' \\
&\quad + \frac{\theta^2 S(s)''^2 v}{C_p(1 + Z_0/Z)} = 0, \\
&m(\ddot{w} + \dot{\Omega}v + 2\Omega\dot{v} - \Omega^2 w) - j(\Omega^2 w'' + \ddot{w}'') \\
&\quad + EI[w'(v'v'' + w'w'')' + w''']' + c\dot{w} \\
&\quad + \frac{1}{2}m\left\{ w' \int_L^s \frac{\partial^2}{\partial t^2}\left[\int_0^s (v'^2 + w'^2)\mathrm{d}s\right]\mathrm{d}s \right\}' \\
&\quad + \frac{\theta^2 S(s)''^2 w}{C_p(1 + Z_0/Z)} = 0.
\end{aligned} \tag{24}$$

Introducing dimensionless variables and parameters

$$\begin{aligned}
&s^* = \frac{s}{L}, \quad v^* = \frac{v}{L}, \quad w^* = \frac{w}{L}, \quad t^* = \tau t, \\
&J = \frac{j}{mL^2}, \quad \tau = \sqrt{\frac{EI}{mL^4}}, \quad \Omega^* = \frac{\Omega}{\tau}, \\
&c^* = \frac{c}{m\tau}, \quad \kappa = \frac{\theta^2}{mC_p L^4 \tau^2}.
\end{aligned} \tag{25}$$

Substituting Eq. (25) into Eq. (24), the dimensionless form of the governing equations becomes

$$\begin{aligned}
&\ddot{v} - \dot{\Omega}w - 2\Omega\dot{w} - \Omega^2 v - J\Omega^2 v'' - J\ddot{v}'' \\
&\quad + [v'(v'v'' + w'w'')' + v''']' + c\dot{v} \\
&\quad + \frac{1}{2}\left\{ v' \int_1^s \frac{\partial^2}{\partial t^2}\left[\int_0^s (v'^2 + w'^2)\mathrm{d}s\right]\mathrm{d}s \right\}' \\
&\quad + \frac{\kappa S(s)''^2 v}{1 + Z_0/Z} = 0, \\
&\ddot{w} + \dot{\Omega}v + 2\Omega\dot{v} - \Omega^2 w - J\Omega^2 w'' - J\ddot{w}'' \\
&\quad + [w'(v'v'' + w'w'')' + w''']' + c\dot{w} \\
&\quad + \frac{1}{2}\left\{ w' \int_1^s \frac{\partial^2}{\partial t^2}\left[\int_0^s (v'^2 + w'^2)\mathrm{d}s\right]\mathrm{d}s \right\}' \\
&\quad + \frac{\kappa S(s)''^2 w}{1 + Z_0/Z} = 0.
\end{aligned} \tag{26}$$

By neglecting the terms of the rotary inertia and geometric non-linearity, our governing Eq. (26) can recover those equations in Refs. [1, 2] that focused on the linear counterpart of the piezoelectric gyroscope. In contrast to the nonlinear shaft models [42, 48], which studied only a rotating beam without piezoelectric materials, two additional piezoelectric coupling terms ($\kappa S(s)''^2 v/(1 + Z_0/Z)$ and $\kappa S(s)''^2 w/(1 + Z_0/Z)$) and different linear terms such as gyroscopic coupling terms and centrifugal force terms are presented in the current formulation for an investigation.

In this study, considering the simply-supported boundary condition ($v = w = 0$ and $v'' = w'' = 0$) at both ends, we use Galerkin method and the appropriate sine function

$$\begin{aligned} v(s,t) &= q(t)\sin(n\pi s), \\ w(s,t) &= p(t)\sin(n\pi s), \end{aligned} \tag{27}$$

where n is the mode number, p and q are generalized temporal coordinates and coupled to each other. Substituting Eq. (27) into Eq. (26), letting $L_1 = 0$, $L_2 = L$, and assuming a constant base angular speed Ω, we can obtain two non-linear ordinary differential equations

$$\begin{aligned} &(1 + Jn^2\pi^2)\ddot{q} - 2\Omega\dot{p} + cn^4\pi^4\dot{q} \\ &\quad + \left(n^4\pi^4 - \Omega^2 + J\Omega^2 n^2\pi^2 + \frac{\kappa n^4\pi^4}{1 + Z_0/Z}\right)q + n^6\pi^6 q^3 \\ &\quad + n^6\pi^6 qp^2 - \left(\frac{3}{8}n^2\pi^2 - \frac{1}{3}n^4\pi^4\right)(q\dot{q}^2 + q\dot{p}^2 \\ &\quad + qp\ddot{p} + q^2\ddot{q}) = 0, \\ &(1 + Jn^2\pi^2)\ddot{p} + 2\Omega\dot{q} + cn^4\pi^4\dot{p} \\ &\quad + \left(n^4\pi^4 - \Omega^2 + J\Omega^2 n^2\pi^2 + \frac{\kappa n^4\pi^4}{1 + Z_0/Z}\right)p + n^6\pi^6 p^3 \\ &\quad + n^6\pi^6 pq^2 - \left(\frac{3}{8}n^2\pi^2 - \frac{1}{3}n^4\pi^4\right)(p\dot{p}^2 \\ &\quad + p\dot{q}^2 + qp\ddot{q} + p^2\ddot{p}) = 0. \end{aligned} \tag{28}$$

3 Analysis of the linear frequency and responses to initial conditions

In this section, the free vibration of the linear part of Eq. (28) is studied first. Neglecting damping and non-linear terms, one can obtain two second-order linear ordinary differential equations with respect to t

$$\boldsymbol{M}\ddot{\boldsymbol{Q}} + \boldsymbol{G}\dot{\boldsymbol{Q}} + \boldsymbol{K}\boldsymbol{Q} = 0, \tag{29}$$

with

$$\begin{aligned} &\boldsymbol{Q} = \begin{bmatrix} q & p \end{bmatrix}^{\mathrm{T}}, \ \boldsymbol{M} = \begin{bmatrix} 1 + Jn^2\pi^2 & 0 \\ 0 & 1 + Jn^2\pi^2 \end{bmatrix}, \ \boldsymbol{G} = \begin{bmatrix} 0 & -2\Omega \\ 2\Omega & 0 \end{bmatrix}, \\ &\boldsymbol{K} = \begin{bmatrix} n^4\pi^4 - \Omega^2 + J\Omega^2 n^2\pi^2 + \frac{\kappa n^4\pi^4}{1+Z/Z_0} & 0 \\ 0 & n^4\pi^4 - \Omega^2 + J\Omega^2 n^2\pi^2 + \frac{\kappa n^4\pi^4}{1+Z/Z_0} \end{bmatrix}. \end{aligned} \tag{30}$$

Substituting $\boldsymbol{Q} = \boldsymbol{\mu} e^{i\omega t}$ into Eq. (29), and according to the boundary conditions, the natural frequencies based on the linear system can be obtained as

$$\omega_{f,b} = \frac{\pm\Omega + \sqrt{(1 + Jn^2\pi^2)\left[n^4\pi^4 - \Omega^2 + J\Omega^2 n^2\pi^2 + \kappa n^4\pi^4/(1 + Z_0/Z)\right] + \Omega^2}}{1 + Jn^2\pi^2}. \tag{31}$$

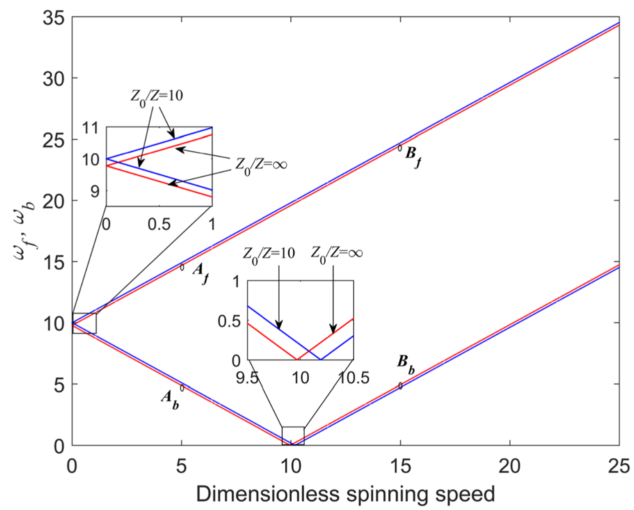

Fig. 3 Natural frequencies versus spinning speed ($J = 0.002$, $n = 1$, $\kappa = 0.5$, and $c = 0$)

Then, the corresponding column vector $\boldsymbol{\mu}$ can be obtained by substituting ω_f and ω_b of Eq. (31) back into Eq. (29). The column vector $\boldsymbol{\mu}$ is different when Ω greater or smaller than a critical value

$$\boldsymbol{\mu} = \begin{cases} \begin{bmatrix} -\mathrm{i} & \mathrm{i} \\ 1 & 1 \end{bmatrix}, & \text{when} \quad \Omega < n^2\pi^2\sqrt{\dfrac{1 + \kappa/(1 + Z_0/Z)}{1 - Jn^2\pi^2}}, \\ \begin{bmatrix} -\mathrm{i} & -\mathrm{i} \\ 1 & 1 \end{bmatrix}, & \text{when} \quad \Omega > n^2\pi^2\sqrt{\dfrac{1 + \kappa/(1 + Z_0/Z)}{1 - Jn^2\pi^2}}, \end{cases} \tag{32}$$

where the first column $[-\mathrm{i}\ 1]^{\mathrm{T}}$ corresponding to ω_f represents forward precession and the second column $[\mathrm{i}\ 1]^{\mathrm{T}}$ corresponding to ω_b represents backward precession in the sub-critical case. On the critical value there exists a switch point of the first mode from backward precession to forward precession. Beyond the critical point, both modes are forward precession.

The two scalar equations of Eq. (29) are only linearly gyroscopic coupled by neglecting the non-linear terms and damping. In Fig. 3, the first two natural frequencies versus spinning speeds are plotted for electrical resistance $Z_0/Z = 10$ and $Z_0/Z = \infty$ with parameters $J = 0.002$, $n = 1$, $\kappa = 0.5$, and $c = 0$. For each value of Z, two natural frequencies correspond to the two gyroscopic modes of the spinning piezoelectric beam. Figure 3 shows that the forward frequency ω_f increases and the backward frequency ω_b decreases, followed by an increase after the critical point. In the local amplified plot, there are no electric fields in both directions for the case of shortened electrodes ($Z_0/Z = \infty$). In this case, the piezoelectric coupling effect related to electric fields does not

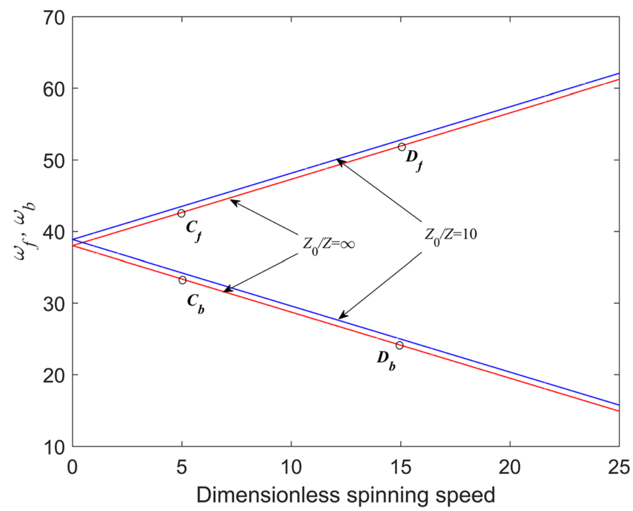

Fig. 4 Natural frequencies versus spinning speed ($J=0.002$, $n=2$, $\kappa=0.5$, and $c=0$)

exist. When the electrodes are not shortened ($Z_0/Z=10$), as presented in Fig. 3, there are electric energy transfers in the two directions, which causes stiffening of the spinning piezoelectric beam, and higher frequencies are found. Figure 3 also shows that the frequency ω_b is decreasing first, and then increasing, and there exists a critical switch value. When the electrodes are not shortened ($Z_0/Z=10$), the point of critical value is pushed back compared with the shortened case ($Z_0/Z=\infty$), although the effect of the electrodes is weak. Similarly, Fig. 4 shows the second two natural frequencies versus spinning speeds, which are plotted for $Z_0/Z=10$ and $Z_0/Z=\infty$ with parameters $J=0.002$, $n=2$, $\kappa=0.5$, and $c=0$. When shortened electrodes ($Z_0/Z=\infty$) are considered, there exist neither electric fields nor piezoelectric coupling effect. When the electrodes are not shortened ($Z_0/Z=10$), electric field appears causing higher frequencies. We will further explain the dynamics of the four typical points $A_{f,b}$, $B_{f,b}$, $C_{f,b}$, and $D_{f,b}$ on Figs. 3 and 4 in the analysis of modal motions in the next section.

4 Application of multiple scales method for the non-linear system

The method of multiple scales is extensively used in this study of gyroscopic system. Now we treat the non-linear gyroscopic system Eq. (28) by using the procedure of the multiple scales method. Then, the solutions of Eq. (28) are assumed as

$$\begin{aligned} q &= \varepsilon q_1(T_0, T_2) + \varepsilon^3 q_3(T_0, T_2) + \cdots, \\ p &= \varepsilon p_1(T_0, T_2) + \varepsilon^3 p_3(T_0, T_2) + \cdots, \end{aligned} \tag{33}$$

where ε is a bookkeeping device denoting small parameter, and the fast and slow time scale $T_0=t$ and $T_2=\varepsilon^2 t$ are introduced. Damping c is scaled with $c\varepsilon^2$ since it is usually very weak. The time derivatives can be written as

$$\frac{\partial}{\partial t} = D_0 + \varepsilon^2 D_2 + \cdots, \quad \frac{\partial}{\partial t^2} = D_0^2 + 2\varepsilon^2 D_2 D_0 + \cdots, \tag{34}$$

with $D_0=\partial/\partial T_0$, $D_2=\partial/\partial T_2$.

Substituting Eqs. (33) and (34) into Eq. (28) and equating the coefficient of different orders of ε yields

$$\begin{aligned} &(1+Jn^2\pi^2)D_0^2 q_1 - 2\Omega D_0 p_1 + [n^4\pi^4 - \Omega^2 \\ &\quad + J\Omega^2 n^2\pi^2 + \kappa n^4\pi^4/(1+Z_0/Z)]q_1 = 0, \\ &(1+Jn^2\pi^2)D_0^2 p_1 + 2\Omega D_0 q_1 + [n^4\pi^4 - \Omega^2 \\ &\quad + J\Omega^2 n^2\pi^2 + \kappa n^4\pi^4/(1+Z_0/Z)]p_1 = 0, \end{aligned} \tag{35}$$

$$\begin{aligned} &(1+Jn^2\pi^2)D_0^2 q_3 - 2\Omega D_0 p_3 + \left[n^4\pi^4 - \Omega^2 \right. \\ &\quad \left. + J\Omega^2 n^2\pi^2 + \kappa n^4\pi^4/(1+Z_0/Z)\right] q_3 \\ &\quad = -cD_0 q_1 + 2\Omega D_2 p_1 - 2(1+Jn^2\pi^2)D_0 D_2 q_1 \\ &\quad - n^6\pi^6(q_1^3 + q_1 p_1^2) + \left(\frac{3}{8}n^2\pi^2 - \frac{1}{3}n^4\pi^4\right)\left[q_1^2 D_0^2 q_1 \right. \\ &\quad \left. + q_1(D_0 q_1)^2 + q_1(D_0 p_1)^2 + q_1 p_1 D_0^2 p_1\right], (1+Jn^2\pi^2)D_0^2 p_3 \\ &\quad + 2\Omega D_0 q_3 + \left[n^4\pi^4 - \Omega^2 + J\Omega^2 n^2\pi^2 + \kappa n^4\pi^4/(1+Z_0/Z)\right]p_3 \\ &\quad = -cD_0 p_1 - 2\Omega D_2 q_1 - 2(1+Jn^2\pi^2)D_0 D_2 p_1 \\ &\quad - n^6\pi^6(p_1^3 + p_1 q_1^2) + \left(\frac{3}{8}n^2\pi^2 - \frac{1}{3}n^4\pi^4\right)\left[p_1^2 D_0^2 p_1 \right. \\ &\quad \left. + p_1(D_0 q_1)^2 + p_1(D_0 p_1)^2 + q_1 p_1 D_0^2 q_1\right]. \end{aligned} \tag{36}$$

For the sub-critical case, $\Omega < n^2\pi^2\sqrt{\frac{1+\kappa/(1+Z_0/Z)}{1-Jn^2\pi^2}}$, the solutions to Eq. (35) are assumed as

$$\begin{aligned} q_1(T_0, T_2) &= -\mathrm{i}A_1(T_2)\mathrm{e}^{\mathrm{i}\omega_f T_0} + \mathrm{i}A_2(T_2)\mathrm{e}^{\mathrm{i}\omega_b T_0} \\ &\quad + \mathrm{i}\bar{A}_1(T_2)\mathrm{e}^{-\mathrm{i}\omega_f T_0} - \mathrm{i}\bar{A}_2(T_2)\mathrm{e}^{-\mathrm{i}\omega_b T_0}, \\ p_1(T_0, T_2) &= A_1(T_2)\mathrm{e}^{\mathrm{i}\omega_f T_0} + A_2(T_2)\mathrm{e}^{\mathrm{i}\omega_b T_0} \\ &\quad + \bar{A}_1(T_2)\mathrm{e}^{-\mathrm{i}\omega_f T_0} + \bar{A}_2(T_2)\mathrm{e}^{-\mathrm{i}\omega_b T_0}. \end{aligned} \tag{37}$$

Substituting Eq. (37) into Eq. (36), one can obtain

$$\begin{aligned} &(1+Jn^2\pi^2)D_0^2 q_3 - 2\Omega D_0 p_3 + \left[n^4\pi^4 - \Omega^2 \right. \\ &\quad \left. + J\Omega^2 n^2\pi^2 + \kappa n^4\pi^4/(1+Z_0/Z)\right]q_3 \\ &\quad = F_1(T_2)\mathrm{e}^{\mathrm{i}\omega_f T_0} + B_1(T_2)\mathrm{e}^{\mathrm{i}\omega_b T_0} + cc + nst, \\ &(1+Jn^2\pi^2)D_0^2 p_3 + 2\Omega D_0 q_3 + \left[n^4\pi^4 - \Omega^2 \right. \\ &\quad \left. + J\Omega^2 n^2\pi^2 + \kappa n^4\pi^4/(1+Z_0/Z)\right]p_3 \\ &\quad = F_2(T_2)\mathrm{e}^{\mathrm{i}\omega_f T_0} + B_2(T_2)\mathrm{e}^{\mathrm{i}\omega_b T_0} + cc + nst, \end{aligned} \tag{38}$$

where "*nst*" denotes non-secular terms, "*cc*" denotes the conjugate of the proceeding terms, and

$$
\begin{aligned}
F_1(T_2) &= -2(\omega_f + Jn^2\pi^2\omega_f - \Omega)D_2A_1(T_2) \\
&\quad - c\omega_f A_1(T_2) + 4\mathrm{i}n^6\pi^6\bar{A}_1(T_2)A_1^2(T_2) \\
&\quad + \frac{1}{2}\mathrm{i}(\Gamma_1 + 16n^6\pi^6)A_1(T_2)\bar{A}_2(T_2)A_2(T_2), \\
B_1(T_2) &= 2(\omega_b + Jn^2\pi^2\omega_b + \Omega)D_2A_2(T_2) \\
&\quad + c\omega_b A_2(T_2) - 4\mathrm{i}n^6\pi^6\bar{A}_2(T_2)A_2^2(T_2) \\
&\quad - \frac{1}{2}\mathrm{i}(\Gamma_1 + 16n^6\pi^6)A_1(T_2)A_2(T_2)\bar{A}_1(T_2), \\
F_2(T_2) &= -2\mathrm{i}(\omega_f + Jn^2\pi^2\omega_f - \Omega)D_2A_1(T_2) \\
&\quad - c\mathrm{i}\omega_f A_1(T_2) - 4n^6\pi^6\bar{A}_1(T_2)A_1^2(T_2) \\
&\quad - \frac{1}{2}(\Gamma_1 + 16n^6\pi^6)A_1(T_2)A_2(T_2)\bar{A}_2(T_2), \\
B_2(T_2) &= -2\mathrm{i}(\omega_b + Jn^2\pi^2\omega_b + \Omega)D_2A_2(T_2) \\
&\quad - c\mathrm{i}\omega_b A_2(T_2) - 4n^6\pi^6\bar{A}_2(T_2)A_2^2(T_2) \\
&\quad - \frac{1}{2}(\Gamma_1 + 16n^6\pi^6)A_1(T_2)A_2(T_2)\bar{A}_1(T_2), \\
\Gamma_1 &= \left(\frac{3}{2}n^2\pi^2 - \frac{4}{3}n^4\pi^4\right)(\omega_f + \omega_b)^2.
\end{aligned}
$$

To determine the solvability conditions of gyroscopic ordinary differential Eq. (38), q_3 and p_3 are expressed as

$$
\begin{aligned}
q_3(T_0, T_2) &= A_{11}(T_2)\mathrm{e}^{\mathrm{i}\omega_f T_0} + A_{12}(T_2)\mathrm{e}^{\mathrm{i}\omega_b T_0}, \\
\mathrm{p}_3(T_0, T_2) &= A_{21}(T_2)\mathrm{e}^{\mathrm{i}\omega_f T_0} + A_{22}(T_2)\mathrm{e}^{\mathrm{i}\omega_b T_0}.
\end{aligned}
\tag{40}
$$

Substituting Eq. (40) into Eq. (39) and equating the coefficient of $\mathrm{e}^{\mathrm{i}\omega_f T_0}$, we obtain

$$
\begin{aligned}
&\left[-\omega_f^2 - Jn^2\pi^2\omega_f^2 - \Omega^2 + n^4\pi^4 + J\Omega^2n^2\pi^2 + \kappa n^4\pi^4/(1 + Z_0/Z)\right]A_{11}(T_2) \\
&\quad - 2\mathrm{i}\omega_f\Omega A_{21}(T_2) = F_1(T_2), \\
&\left[-\omega_f^2 - Jn^2\pi^2\omega_f^2 - \Omega^2 + n^4\pi^4 + J\Omega^2n^2\pi^2 + \kappa n^4\pi^4/(1 + Z_0/Z)\right]A_{21}(T_2) \\
&\quad + 2\mathrm{i}\omega_f\Omega A_{11}(T_2) = F_2(T_2).
\end{aligned}
\tag{41}
$$

Similarly, for coefficient of $\mathrm{e}^{\mathrm{i}\omega_b T_0}$, the following equations are obtained

$$
\begin{aligned}
&\left[-\omega_b^2 - Jn^2\pi^2\omega_b^2 - \Omega^2 + n^4\pi^4 + J\Omega^2n^2\pi^2 + \kappa n^4\pi^4/(1 + Z_0/Z)\right]A_{12}(T_2) \\
&\quad - 2\mathrm{i}\omega_b\Omega A_{22}(T_2) = B_1(T_2), \\
&\left[-\omega_b^2 - Jn^2\pi^2\omega_b^2 - \Omega^2 + n^4\pi^4 + J\Omega^2n^2\pi^2 + \kappa n^4\pi^4/(1 + Z_0/Z)\right]A_{22}(T_2) \\
&\quad + 2\mathrm{i}\omega_b\Omega A_{12}(T_2) = B_2(T_2).
\end{aligned}
\tag{42}
$$

Equations (41) and (42) are composed of algebraic equations with respect to $A_{11}(T_2)$, $A_{21}(T_2)$ and $A_{12}(T_2)$, $A_{22}(T_2)$. The nontrivial condition can be expressed as [42]

$$
\begin{aligned}
&\begin{vmatrix} -\omega_f^2 - Jn^2\pi^2\omega_f^2 - \Omega^2 + n^4\pi^4 + J\Omega^2n^2\pi^2 + \kappa n^4\pi^4/(1 + Z_0/Z) & F_1(T_2) \\ 2\mathrm{i}\omega_f\Omega & F_2(T_2) \end{vmatrix} = 0, \\
&\begin{vmatrix} -\omega_b^2 - Jn^2\pi^2\omega_b^2 - \Omega^2 + n^4\pi^4 + J\Omega^2n^2\pi^2 + \kappa n^4\pi^4/(1 + Z_0/Z) & B_1(T_2) \\ 2\mathrm{i}\omega_b\Omega & B_2(T_2) \end{vmatrix} = 0.
\end{aligned}
\tag{43}
$$

After some mathematical manipulations, the solvability conditions can be written as

$$
\begin{aligned}
&\mathrm{i}\Lambda_1D_2A_1(T_2) + 2\mathrm{i}c\omega_f A_1(T_2) + (\Gamma_1 + 16n^6\pi^6)A_1(T_2)\bar{A}_2(T_2)A_2(T_2) \\
&\quad + 8n^6\pi^6\bar{A}_1(T_2)A_1(T_2)^2 = 0, \\
&\mathrm{i}\Lambda_2D_2A_2(T_2) + 2\mathrm{i}c\omega_b A_2(T_2) + (\Gamma_1 + 16n^6\pi^6)A_2(T_2)\bar{A}_1(T_2)A_1(T_2) \\
&\quad + 8n^6\pi^6\bar{A}_2(T_2)A_2(T_2)^2 = 0,
\end{aligned}
\tag{44}
$$

with

$$
\Lambda_1 = 4(\omega_f + Jn^2\pi^2\omega_f - \Omega), \quad \Lambda_2 = 4(\omega_b + Jn^2\pi^2\omega_b + \Omega).
\tag{45}
$$

For the super-critical case, $\Omega > n^2\pi^2\sqrt{\frac{1+\kappa/(1+Z_0/Z)}{1-Jn^2\pi^2}}$, the solutions of Eq. (35) are assumed

$$
\begin{aligned}
\mathrm{q}_1(T_0, T_2) &= -\mathrm{i}A_1(T_2)\mathrm{e}^{\mathrm{i}\omega_f T_0} - \mathrm{i}A_2(T_2)\mathrm{e}^{\mathrm{i}\omega_b T_0} \\
&\quad + \mathrm{i}\bar{A}_1(T_2)\mathrm{e}^{-\mathrm{i}\omega_f T_0} + \mathrm{i}\bar{A}_2(T_2)\mathrm{e}^{-\mathrm{i}\omega_b T_0}, \\
p_1(T_0, T_2) &= A_1(T_2)\mathrm{e}^{\mathrm{i}\omega_f T_0} + A_2(T_2)\mathrm{e}^{\mathrm{i}\omega_b T_0} \\
&\quad + \bar{A}_1(T_2)\mathrm{e}^{-\mathrm{i}\omega_f T_0} + \bar{A}_2(T_2)\mathrm{e}^{-\mathrm{i}\omega_b T_0}.
\end{aligned}
\tag{46}
$$

Similarly, the solvability conditions are derived as

$$
\begin{aligned}
&\mathrm{i}\Lambda_1D_2A_1(T_2) + 2\mathrm{i}c\omega_f A_1(T_2) + (\Gamma_2 + 16n^6\pi^6)A_1(T_2)\bar{A}_2(T_2)A_2(T_2) \\
&\quad + 8n^6\pi^6\bar{A}_1(T_2)A_1(T_2)^2 = 0, \\
&\mathrm{i}\Lambda_3D_2A_2(T_2) + 2\mathrm{i}c\omega_b A_2(T_2) + (\Gamma_2 + 16n^6\pi^6)A_1(T_2)\bar{A}_1(T_2)A_2(T_2) \\
&\quad + 8n^6\pi^6\bar{A}_2(T_2)A_2(T_2)^2 = 0,
\end{aligned}
\tag{47}
$$

where

$$
\Gamma_2 = \left(\frac{3}{2}n^2\pi^2 - \frac{4}{3}n^4\pi^4\right)(\omega_f - \omega_b)^2, \quad \Lambda_3 = 4(\omega_b + Jn^2\pi^2\omega_b - \Omega).
\tag{48}
$$

For both the sub-critical and super-critical cases, slow-varying complex amplitudes A_1 and A_2 are expressed in polar form

$$
A_1(T_2) = \frac{1}{2}a_1(T_2)\mathrm{e}^{\mathrm{i}\gamma_1(T_2)}, \quad A_2(T_2) = \frac{1}{2}a_2(T_2)\mathrm{e}^{\mathrm{i}\gamma_2(T_2)},
\tag{49}
$$

where $a_1(T_2)$, $a_2(T_2)$ and $\gamma_1(T_2)$, $\gamma_2(T_2)$ are real amplitudes and phases of the response, respectively.

When $\Omega < n^2\pi^2\sqrt{\frac{1+\kappa/(1+Z_0/Z)}{1-Jn^2\pi^2}}$, substituting Eq. (49) into Eq. (44), and separating real part and imaginary part, the slow-varying amplitudes and phases can be obtained as

$$
\begin{aligned}
&\frac{1}{2}\Lambda_1 D_2 a_1(T_2) + c\omega_f a_1(T_2) = 0,\\
&\frac{1}{2}\Lambda_2 D_2 a_2(T_2) + c\omega_b a_2(T_2) = 0,\\
&\quad -\frac{1}{2}\Lambda_1 a_1(T_2) D_2\gamma_1(T_2)\\
&\quad +\frac{1}{8}(\Gamma_1 + 16n^6\pi^6) a_1(T_2) a_2^2(T_2) + n^6\pi^6 a_1^3(T_2) = 0,\\
&\quad -\frac{1}{2}\Lambda_2 a_2(T_2) D_2\gamma_2(T_2) + \frac{1}{8}(\Gamma_1 + 16n^6\pi^6) a_2(T_2) a_1^2(T_2)\\
&\quad + n^6\pi^6 a_2^3(T_2) = 0.
\end{aligned}
\tag{50}
$$

Substituting the first two equations of Eq. (50) for $a_1(T_2)$ and $a_2(T_2)$

$$
a_1(T_2) = C_1 \mathrm{e}^{-2c\omega_f T_2/\Lambda_1}, \quad a_2(T_2) = C_2 \mathrm{e}^{-2c\omega_b T_2/\Lambda_2}, \tag{51}
$$

into the last two equations of Eq. (50), $\gamma_1(T_2)$ and $\gamma_2(T_2)$ can be obtained as

$$
\begin{aligned}
\gamma_1(T_2) &= -\frac{C_2^2(\Gamma_1 + 16n^6\pi^6)\Lambda_2 \mathrm{e}^{-4c\omega_b T_2/\Lambda_2}}{16\Lambda_1 c\omega_b} - \frac{C_1^2 n^2\pi^2 \mathrm{e}^{-4c\omega_f T_2/\Lambda_1}}{2c\omega_f} + C_4,\\
\gamma_2(T_2) &= -\frac{C_1^2(\Gamma_1 + 16n^6\pi^6)\Lambda_1 \mathrm{e}^{-4c\omega_f T_2/\Lambda_1}}{16\Lambda_2 c\omega_f} - \frac{C_2^2 n^2\pi^2 \mathrm{e}^{-4c\omega_b T_2/\Lambda_2}}{2c\omega_b} + C_3.
\end{aligned}
\tag{52}
$$

where C_1–C_4 are constants determined by initial conditions. Substituting Eqs. (51) and (52) into Eq. (49), and using the results into Eq. (37), we obtain the approximate analytical solutions

$$
\begin{aligned}
v(s,t) = \sin(n\pi s)[&B_f \sin(B_1 B_b^2 + B_2 B_f^2 + \omega_f T_0 + C_4)\\
&- \mathrm{i}B_f \cos(B_1 B_b^2 + B_2 B_f^2 + \omega_f T_0 + C_4)\\
&- B_b \sin(B_3 B_f^2 + B_4 B_b^2 + \omega_b T_0 + C_3)\\
&+ \mathrm{i}B_b \cos(B_3 B_f^2 + B_4 B_b^2 + \omega_b T_0 + C_3)],\\
w(s,t) = \sin(n\pi s)[&B_f \cos(B_1 B_b^2 + B_2 B_f^2 + \omega_f T_0 + C_4)\\
&+ \mathrm{i}B_f \sin(B_1 B_b^2 + B_2 B_f^2 + \omega_f T_0 + C_4)\\
&+ B_b \cos(B_3 B_f^2 + B_4 B_b^2 + \omega_b T_0 + C_3)\\
&+ \mathrm{i}B_b \sin(B_3 B_f^2 + B_4 B_b^2 + \omega_b T_0 + C_3)],
\end{aligned}
\tag{53}
$$

with

$$
\begin{aligned}
&B_f = C_1 \mathrm{e}^{\frac{-2c\omega_f T_0}{\Lambda_1}}, \quad B_b = C_2 \mathrm{e}^{\frac{-2c\omega_b T_0}{\Lambda_2}},\\
&B_1 = -\frac{(\Gamma_1 + 16n^6\pi^6)\Lambda_2}{16\Lambda_1 c\omega_b}, \quad B_2 = -\frac{n^6\pi^6}{2c\omega_f},\\
&B_3 = -\frac{(\Gamma_1 + 16n^6\pi^6)\Lambda_1}{16\Lambda_2 c\omega_f}, \quad B_4 = -\frac{n^6\pi^6}{2c\omega_b}.
\end{aligned}
\tag{54}
$$

When $\Omega > n^2\pi^2\sqrt{\frac{1+\kappa/(1+Z_0/Z)}{1-Jn^2\pi^2}}$, similarly, the approximate analytical solutions can be obtained as

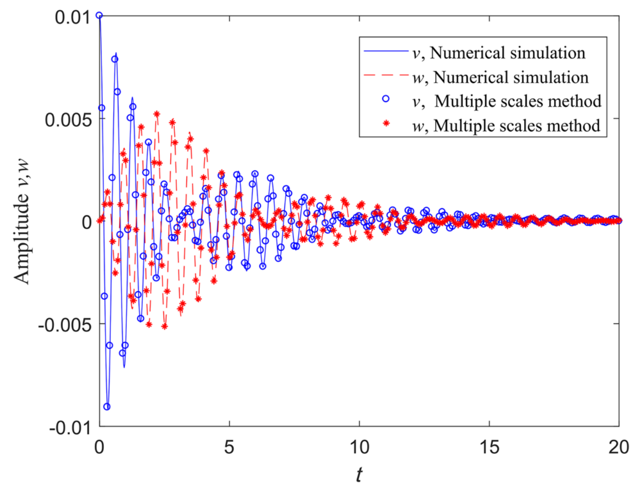

Fig. 5 Time history for Ω=0.5, J=0.002, κ=0.5, Z_0/Z=10, and c=0.005

$$
\begin{aligned}
v(s,t) = \sin(n\pi s)[&B_f \sin(B_1 B_b^2 + B_2 B_f^2 + \omega_f T_0 + C_4)\\
&- \mathrm{i}B_f \cos(B_1 B_b^2 + B_2 B_f^2 + \omega_f T_0 + C_4)\\
&+ B_b \sin(B_3 B_f^2 + B_4 B_b^2 + \omega_b T_0 + C_3)\\
&- \mathrm{i}B_b \cos(B_3 B_f^2 + B_4 B_b^2 + \omega_b T_0 + C_3)],\\
w(s,t) = \sin(n\pi s)[&B_f \cos(B_1 B_b^2 + B_2 B_f^2 + \omega_f T_0 + C_4)\\
&+ \mathrm{i}B_f \sin(B_1 B_b^2 + B_2 B_f^2 + \omega_f T_0 + C_4)\\
&+ B_b \cos(B_3 B_f^2 + B_4 B_b^2 + \omega_b T_0 + C_3)\\
&+ \mathrm{i}B_b \sin(B_3 B_f^2 + B_4 B_b^2 + \omega_b T_0 + C_3)],
\end{aligned}
\tag{55}
$$

where

$$
\begin{aligned}
&B_f = C_1 \mathrm{e}^{\frac{-2c\omega_f T_0}{\Lambda_1}}, \quad B_b = C_2 \mathrm{e}^{\frac{-2c\omega_b T_0}{\Lambda_3}},\\
&B_1 = -\frac{(\Gamma_2 + 16n^6\pi^6)\Lambda_3}{16\Lambda_1 c\omega_b}, \quad B_2 = -\frac{n^6\pi^6}{2c\omega_f},\\
&B_3 = -\frac{(\Gamma_2 + 16n^6\pi^6)\Lambda_1}{16\Lambda_3 c\omega_f}, \quad B_4 = -\frac{n^6\pi^6}{2c\omega_b}.
\end{aligned}
\tag{56}
$$

4.1 Numerical analysis

In this subsection, the numerical simulation will be employed to validate the results by the method of multiple scales [49, 50]. The displacement time histories of the spinning piezoelectric beam based on the gyroscopically coupled non-linear system have been illustrated in Figs. 5 and 6 by both analytical and numerical simulation. The two figures share the same parameters J=0.002, κ=0.5, Z_0/Z=10, and c=0.005, where only the first mode is excited. An initial condition of $v(0)$=0.01, $w(0)$=0, $\dot{v}(0)=0$, and $\dot{w}(0)=0$ in the plane v is used in Fig. 5, by which responses occur

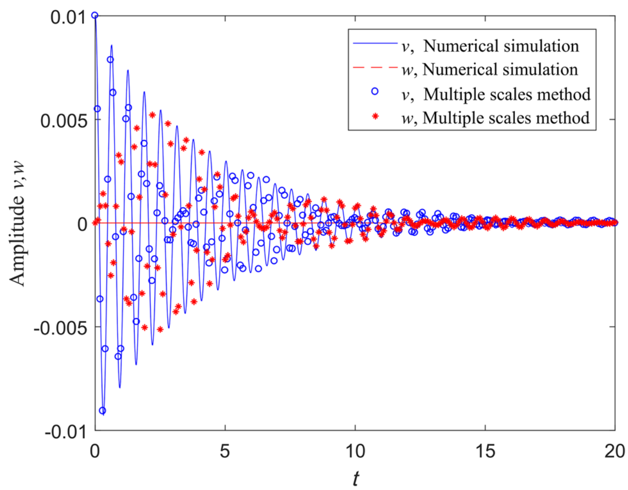

Fig. 6 Time history for $\Omega=0$, $J=0.002$, $\kappa=0.5$, $Z_0/Z=10$, and $c=0.005$

in plane w due to the gyroscopic effect. Since the spinning speed is not high, $\Omega=0.5$, the results of two natural frequencies are close. Hence a beat phenomenon can be located. The displacements of both directions are gradually attenuated until zero because of damping. During the vibration process, the transfer of energy from one direction to another can locate the working mechanism of the piezoelectric vibratory gyroscope. Figure 6 shows the non-spinning case, $\Omega=0.5$: an initial displacement in the plane v is given, where there is no oscillation in plane w because of there is no gyroscope coupling, which is the key role to make the vibratory gyroscopes work.

4.2 Non-linear modal analysis

In this subsection, the modal motions will be discussed. Using the parameters $J=0.002$, $\kappa=0.5$, and $Z_0/Z=\infty$, the non-linear complex mode functions in Eqs. (53) and (55) based on the multiple scales method are shown in Fig. 7. The snapshots for different spinning cases ($\Omega=5$ and $\Omega=15$) in a period of the non-linear spinning piezoelectric beam for the first two orders modal motions are shown in Fig. 7. The modal motions are corresponding to the four typical points $A_{f,b}$, $B_{f,b}$, $C_{f,b}$, and $D_{f,b}$ in Figs. 3 and 4. The first-order modal motions exhibited in Fig. 7a, e are all forward whirling in the sub-critical and supercritical regions, respectively. However, the first-order modal motion exhibited in Fig. 7c is backward whirling in the sub-critical region where the first-order modal motion exhibited in Fig. 7g is forward whirling in the supercritical region. The second-order modal motions of the spinning piezoelectric beam are forward whirling motions as presented in Fig. 7b, f where the second-order modal motions presented in Fig. 7d, h are backward whirling in the sub-critical and supercritical regions.

4.3 Non-linear frequency analysis

It is found that the non-linear frequencies involve two parts in Eqs. (53) and (55). The first part is linear natural frequencies of constants ω_f and ω_b and the second part depends on the slow-varying amplitude $(C_1B_b^2+C_2B_f^2)/T_0$ and $(C_3B_f^2+C_4B_b^2)/T_0$. Therefore, the non-linear natural frequency is a function of J, c, κ, Z_0/Z, and Ω as well as time. Hence, the effect of rotary inertia J, electrical resistance Z_0/Z and spinning speed Ω on the non-linear natural frequencies can be discussed for a specified instant of time (for example $T_0=1$). We can make a definition regarding forward and backward non-linear frequency

$$\omega_{fnl}=C_1B_b^2+C_2B_f^2+\omega_f,\omega_{bnl}=C_3B_f^2+C_4B_b^2+\omega_b, \quad (57)$$

where C_i ($i=1$–4) are coefficients which determined by initial conditions $v(0)=0.01$, $w(0)=0$, $\dot{v}(0)=0$, and $\dot{w}(0)=0$.

The first order amplitude-dependent non-linear frequency is presented in Fig. 8 by using the parameters $J=0.002$, $\kappa=0.5$, $c=0.005$, and $Z_0/Z=10$. The dotted line represents linear frequencies, and the solid line represents non-linear frequencies. It is found that with an increase of the initial amplitudes, the non-linear natural frequencies increase. It is also found that with the increase of the spinning speed, the forward and backward non-linear frequencies all increase.

In Figs. 9 and 10, ω_{fnl} and ω_{bnl} are plotted versus spinning speed Ω for different values of electrical resistance Z_0/Z by using the parameters $J=0.002$, $\kappa=0.5$, and $c=0.005$. In Fig. 9, the first mode ($n=1$) of the forward non-linear frequencies ω_{fnl} increase and the backward frequencies ω_{bnl} decrease first, then increase with the increase of spinning speed for all the values of Z_0/Z. In the local enlarged view, the reduction of electrical resistance causes the higher ω_{fnl}. It is seen that for ω_{bnl}, there exists a local minimum point, the reduction of electrical resistance ($Z_0/Z=\infty$, 10, and 5) causes the higher ω_{bnl} before the minimum point, but the reduction of Z_0/Z causes the lower ω_{bnl} after the minimum point. In Fig. 10, the second mode ($n=2$) of ω_{fnl} increase and ω_{bnl} decrease for all the values of Z_0/Z. From all the figures, we can see the values of ω_{fnl} are larger than ω_{bnl} by using the same parameters.

The non-linear frequencies ω_{fnl} and ω_{bnl} of the first two modes as functions of spinning speed Ω for different rotary inertia J are shown in Figs. 11 and 12 by using the parameters $Z_0/Z=10$, $\kappa=0.5$, and $c=0.005$. It is observed from Figs. 11 and 12 that the essential properties of curves are similar with Figs. 9 and 10 for different rotary inertia J. Figure 11 shows that the reduction of rotary inertia ($J=0.02$, 0.002, and 0.0002) causes the higher ω_{fnl} of the first mode ($n=1$). It is seen that for ω_{bnl}, there exists a local minimum point. Before the local minimum point, the reduction of J

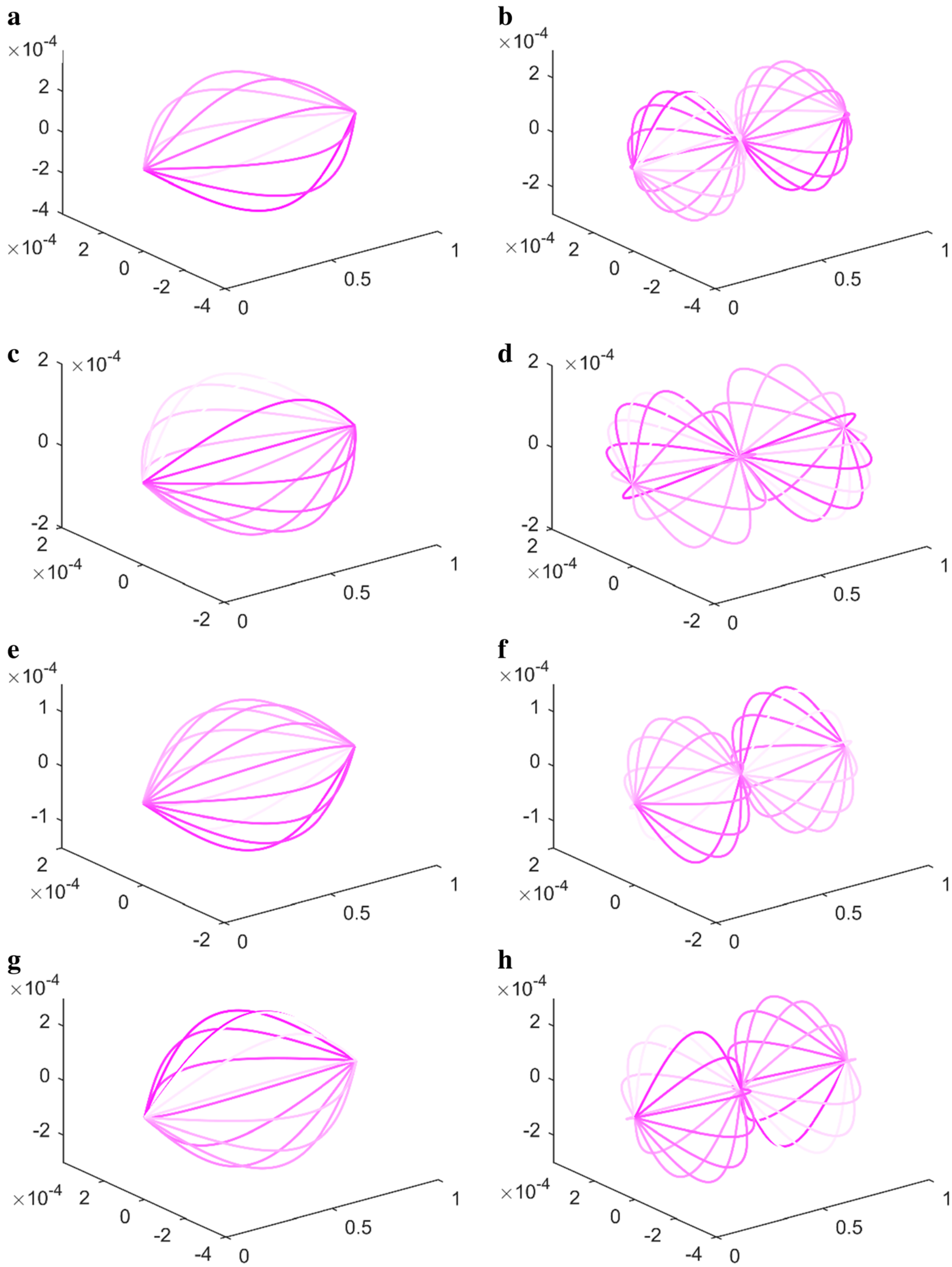

Fig. 7 Complex mode functions derived by the non-linear systems. **a** The first mode (ω_f) when $\Omega=5$, at A_f. **b** The second mode (ω_f) when $\Omega=5$, at C_f. **c** The first mode (ω_b) when $\Omega=5$, at A_b. **d** The second mode (ω_b) when $\Omega=5$, at C_b. **e** The first mode (ω_f) when $\Omega=15$, at B_f. **f** The second mode (ω_f) when $\Omega=15$, at D_f. **g** The first mode (ω_b) when $\Omega=15$, at B_b. **h** The second mode (ω_b) when $\Omega=15$, at D_b

causes the higher ω_{bnl} from $\Omega=0$ to $\Omega=5$, and the reduction of J causes the lower ω_{bnl} from $\Omega=5$ to the minimum point. After the minimum point, the reduction of J causes the higher ω_{bnl}. The reduction of rotary inertia ($J=0.02$, 0.002, and 0.0002) causes the higher ω_{fnl} of the second mode ($n=2$) are shown in Fig. 12. It is found that for ω_{bnl}, there exists a cross-over point. Before the cross-over point, the reduction of J causes the higher ω_{bnl} from $\Omega=0$ to $\Omega=20$, and the reduction of J causes the lower ω_{bnl} from $\Omega=20$ to $\Omega=25$.

The relation of the linear and non-linear frequencies versus Z_0/Z are plotted in Figs. 13 and 14 for $\Omega=1$, 3 by using the parameters $J=0.002$, $\kappa=0.5$, and $c=0.005$. The two figures illustrate that the linear and non-linear frequencies

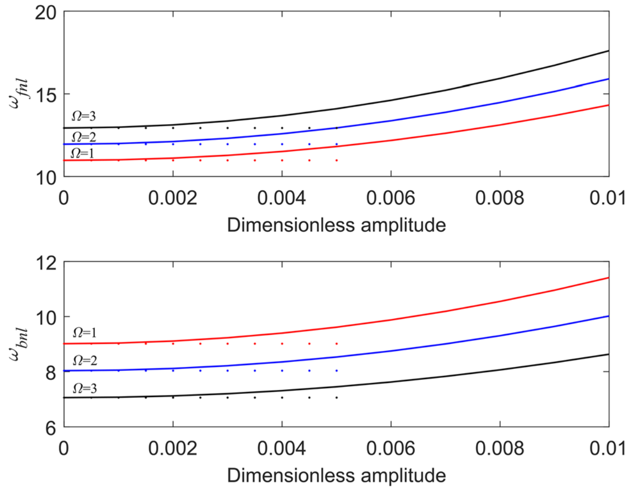

Fig. 8 Non-linear frequencies versus the amplitude ($\kappa=0.5$, $Z_0/Z=10$, $c=0.005$, and $J=0.002$)

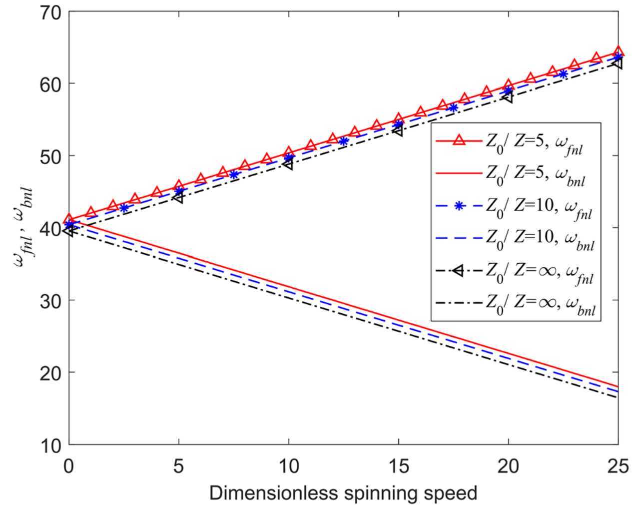

Fig. 10 Non-linear frequencies versus spinning speed ($n=2$, $c=0.005$, $\kappa=0.5$, and $J=0.002$)

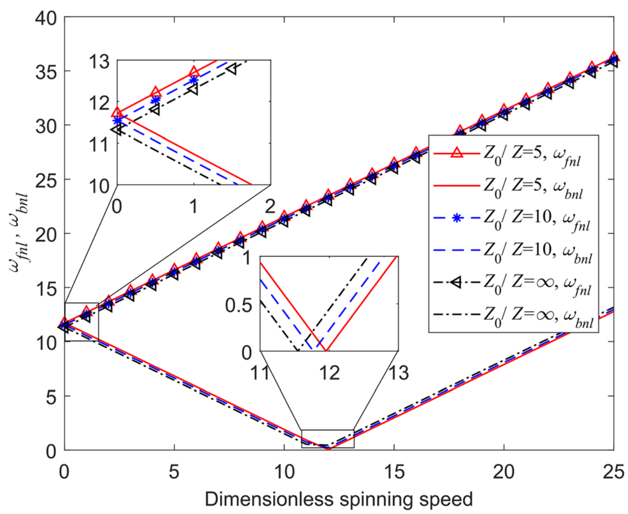

Fig. 9 Non-linear frequencies versus spinning speed ($n=1$, $c=0.005$, $\kappa=0.5$, and $J=0.002$)

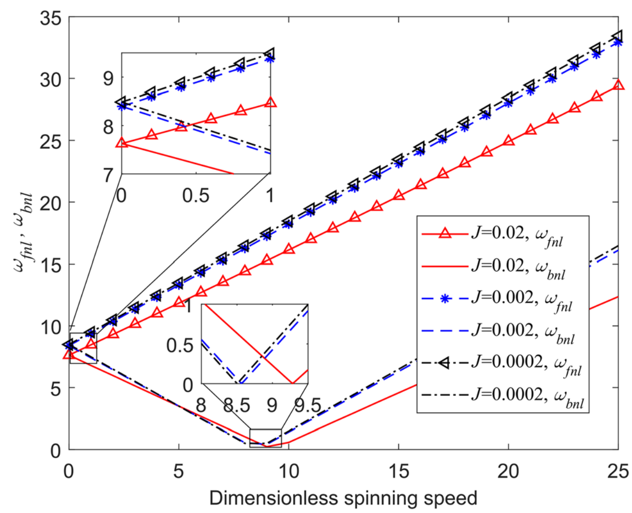

Fig. 11 Non-linear frequencies versus spinning speed ($n=1$, $c=0.005$, $\kappa=0.5$, and $Z_0/Z=10$)

become further apart as the Ω increases. Moreover, the value of linear frequency (e.g. $\Omega=1$, ω_f) is lower than the value of non-linear frequency (e.g. $\Omega=1$, ω_{fnl}) due to the effect of geometric nonlinearities as depicted in Figs. 13 and 14. Further, Fig. 13 shows that the linear and non-linear frequencies vary rapidly according to the small electrical resistance and then become smoothly for the first mode ($n=1$). Together with the dependence of the linear and non-linear frequencies on the spinning speed as shown in Figs. 3 and 9, respectively, the electrical resistance Z_0/Z dependence of non-linear frequencies further complicates the design of the piezoelectric gyroscopes. Figure 14 shows that the linear and non-linear frequencies vary more rapidly than that in Fig. 13 according to the small Z_0/Z and then become smoothly for the second mode ($n=2$). The effect of Z_0/Z for ω_b and ω_{bnl} is greater than ω_f and ω_{fnl}, respectively.

Large vibration of flexible structures leads to high sensitivity of the gyroscopes. However, the non-linear effects should reconsidered in the engineering field of gyroscopes. The clear understanding of varying rules on non-linear frequencies and non-linear normal modes may provide possible optimizations in the vibrating beam gyroscope design, especially for the ones with very flexible structures.

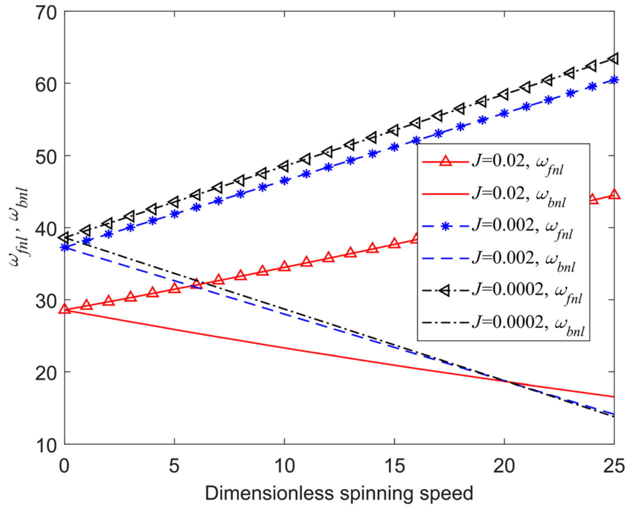

Fig. 12 Non-linear frequencies versus spinning speed ($n=2$, $c=0.005$, $\kappa=0.5$, and $Z_0/Z=10$)

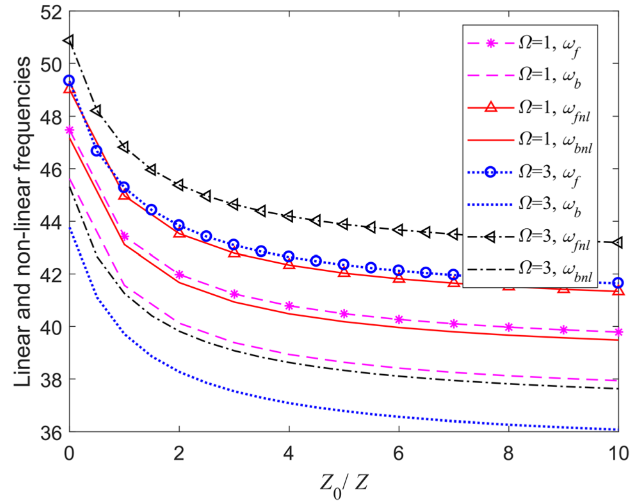

Fig. 14 Linear and non-linear frequencies versus electrical resistance ($n=2$, $c=0.005$, $\kappa=0.5$, and $J=0.002$)

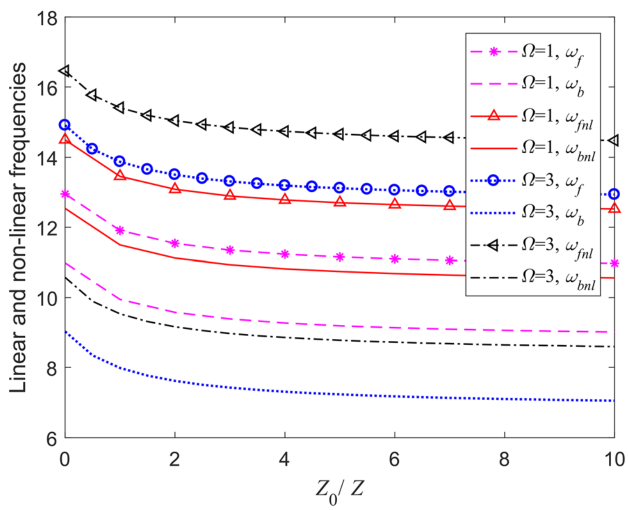

Fig. 13 Linear and non-linear frequencies versus electrical resistance ($n=1$, $c=0.005$, $\kappa=0.5$, and $J=0.002$)

5 Conclusions

The linear and non-linear free vibrations of a spinning piezoelectric beam are investigated by both analytical and numerical simulation. The additional piezoelectric coupling terms and symmetrical governing equations with non-linearities in curvature and inertia of a spinning piezoelectric beam are derived by using extended Hamilton principle and the transformation of two Euler angles. The non-linear frequencies and complex modes are obtained by the multiple scales method. The initial value responses are studied by the analytical method and then validated by numerical method. The main conclusions are highlighted as follows.

1. In the linear and non-linear free vibration analysis of a spinning piezoelectric beam, forward and backward frequencies are studied. The switch of the forward precession and backward precession of the gyroscopic system have been located.
2. The whirling motions of the non-linear complex modes have been illustrated.
3. The electrical resistance (including electromechanical coupling coefficient) should be considered in the field of the piezoelectric spinning beam. The rules of non-linear frequencies varying with electrical resistance, amplitude, and other parameters have been discussed in detail.
4. The investigations of non-linear frequencies and non-linear normal modes provide basic theories needed in the high flexible vibratory gyroscope design.

Acknowledgements This work was supported in part by the National Natural Science Foundation of China (Grants 11672007 and 11832002), Beijing Natural Science Foundation (Grant 3172003), and Graduate Student Science and Technology Foundation of Beijing University of Technology (Grant ykj-2017-00045).

References

1. Yang, J.S., Fang, H.Y.: Analysis of a rotating elastic beam with piezoelectric films as an angular rate sensor. IEEE Trans. Ultrason. Ferroelectr. Freq. Control **49**, 798–804 (2002)

2. Yang, J.S., Fang, H.Y.: A piezoelectric gyroscope based on extensional vibrations of rods. Int. J. Appl. Electromagn. Mech. **17**, 289–300 (2003)
3. Bhadbhade, V., Jahli, N., Mahmoodi, S.N.: A novel piezoelectrically actuated flexural/torsional vibrating beam gyroscope. J. Sound Vib. **311**, 1305–1324 (2008)
4. Lajimi, S.A.M., Heppler, G.R., Abdel-Rahman, E.M.: A mechanical–thermal noise analysis of a nonlinear microgyroscope. Mech. Syst. Signal Process. **83**, 163–175 (2017)
5. Shahgholi, M., Khadem, S.E., Bab, S.: Free vibration analysis of a nonlinear slender rotating shaft with simply support conditions. Mech. Mach. Theory **82**, 128–140 (2014)
6. Nezhad, H.S.A., Hosseini, S.A.A., Zamanian, M.: Flexural–flexural–extensional–torsional vibration analysis of composite spinning shafts with geometrical nonlinearity. Nonlinear Dyn. **89**, 651–690 (2017)
7. Oskouie, M.F., Ansari, R., Sadeghi, F.: Nonlinear vibration analysis of fractional viscoelastic Euler–Bernoulli nanobeams based on the surface stress theory. Acta Mech. Solida Sin. **30**, 416–424 (2017)
8. Zhao, H.S., Zhang, Y., Lie, S.T.: Explicit frequency equations of free vibration of a nonlocal Timoshenko beam with surface effects. Acta Mech. Sin. **34**, 676–688 (2018)
9. Guan, M.J., Liao, W.H.: Design and analysis of a piezoelectric energy harvester for rotational motion system. Energy Convers. Manag. **111**, 239–244 (2016)
10. Zou, H.X., Zhang, W.M., Li, W.B., et al.: Design and experimental investigation of a magnetically coupled vibration energy harvester using two inverted piezoelectric cantilever beams for rotational motion. Energy Convers. Manag. **148**, 1391–1398 (2017)
11. Fang, F., Xia, G.H., Wang, J.G.: Nonlinear dynamic analysis of cantilevered piezoelectric energy harvesters under simultaneous parametric and external excitations. Acta Mech. Sin. **34**, 561–577 (2018)
12. Korayem, M.H., Homayooni, A.: The size-dependent analysis of multilayer micro-cantilever plate with piezoelectric layer incorporated voltage effect based on a modified couple stress theory. Eur. J. Mech. A Solids **61**, 59–72 (2017)
13. Zhang, J.R., Guo, Z.X., Zhang, Y., et al.: Inner structural vibration isolation method for a single control moment gyroscope. J. Sound Vib. **361**, 78–98 (2016)
14. Zhang, D.Y., Xia, Y., Scarpa, F., et al.: Interfacial contact stiffness of fractal rough surfaces. Sci. Rep. **7**, 12874 (2017)
15. He, T., Xie, Y., Shan, Y.C., et al.: Localizing two acoustic emission sources simultaneously using beamforming and singular value decomposition. Ultrasonics **85**, 3–22 (2018)
16. Ding, H., Zhu, M.H., Zhang, Z., et al.: Free vibration of a rotating ring on an elastic foundation. Int. J. Appl. Mech. **9**, 1750051 (2017)
17. Qin, Z., Chu, F., Zu, J.: Free vibrations of cylindrical shells with arbitrary boundary conditions: a comparison study. Int. J. Mech. Sci. **133**, 91–99 (2017)
18. Lang, G.F.: Matrix madness and complex confusion. A review of complex modes from multiple viewpoints. Sound Vib. **46**, 8–12 (2012)
19. Yang, X.D., Yang, J.H., Qian, Y.J., et al.: Dynamics of a beam with both axial moving and spinning motion: an example of bi-gyroscopic continua. Eur. J. Mech. A Solids **69**, 231–237 (2018)
20. Rosenberg, R.M.: The normal modes of nonlinear n-degree-of-freedom systems. ASME J. Appl. Mech. **29**, 7–14 (1962)
21. Nayfeh, A.H., Nayfeh, S.A.: On nonlinear modes of continuous systems. J. Vib. Acoust. **116**, 129–136 (1994)
22. Nayfeh, A.H., Nayfeh, S.A.: Nonlinear normal-modes of a continuous system with quadratic nonlinearities. J. Vib. Acoust. **117**, 199–205 (1995)
23. Shaw, S.W., Pierre, C.: Nonlinear normal-modes and invariant-manifolds. J. Sound Vib. **150**, 170–173 (1991)
24. Shaw, S.W., Pierre, C.: Normal-modes for nonlinear vibratory-systems. J. Sound Vib. **164**, 85–124 (1993)
25. Carlos, E.N.M., César, T.S., Odulpho, G.P.B.N., et al.: Non-linear modal analysis for beams subjected to axial loads: analytical and finite-element solutions. Int. J. Non-Linear Mech. **43**, 551–561 (2008)
26. Uspensky, B., Avramov, K.: Nonlinear modes of piecewise linear systems under the action of periodic excitation. Nonlinear Dyn. **76**, 1151–1156 (2013)
27. Arvin, H., Nejad, F.B.: Non-linear modal analysis of a rotating beam. Int. J. Non-Linear Mech. **46**, 877–897 (2011)
28. Qian, Y.J., Yang, X.D., Wu, H., et al.: Gyroscopic modes decoupling method in parametric instability analysis of gyroscopic systems. Acta Mech. Sin. **34**, 963–969 (2018)
29. Arquier, R., Bellizzi, S., Bouc, R., et al.: Two methods for the computation of nonlinear modes of vibrating systems at large amplitudes. Comput. Struct. **84**, 1565–1576 (2006)
30. Laxalde, D., Thouverez, F.: Complex non-linear modal analysis for mechanical systems: application to turbomachinery bladings with friction interfaces. J. Sound Vib. **322**, 1009–1025 (2009)
31. Kuether, R.J., Allen, M.S.: A numerical approach to directly compute nonlinear normal modes of geometrically nonlinear finite element models. Mech. Syst. Signal Process. **46**, 1–15 (2014)
32. Pesheck, E., Pierre, C., Shaw, S.W.: A new Galerkin-based approach for accurate non-linear normal modes through invariant manifolds. J. Sound Vib. **249**, 971–993 (2002)
33. Renson, L., Deliege, G., Kerschen, G.: An effective finite-element-based method for the computation of nonlinear normal modes of nonconservative systems. Meccanica **49**, 1901–1916 (2014)
34. Pan, Y., Liu, X.D., Shan, Y.C., et al.: Complex modal analysis of serpentine belt drives based on beam coupling model. Mech. Mach. Theory **116**, 162–177 (2017)
35. Qin, Z.Y., Han, Q.K., Chu, F.L.: Analytical model of bolted disk–drum joints and its application to dynamic analysis of jointed rotor. Proc. Inst. Mech. Eng. Part C J. Mech. Eng. Sci. **228**, 646–663 (2014)
36. Hong, J., Yu, P.C., Zhang, D.Y., et al.: Modal characteristics analysis for a flexible rotor with non-smooth constraint due to intermittent rub-impact. Chin. J. Aeronaut. **31**, 498–513 (2018)
37. Sturla, F.A., Argento, A.: Free and forced vibrations of a spinning viscoelastic beam. J. Vib. Acoust. **118**, 463–468 (1996)
38. Ishida, Y., Inoue, T.: Nonstationary oscillations of a nonlinear rotor during acceleration through the major critical speed—influence of internal resonance. JSME Int. J. Ser. C Mech. Syst. Mach. Elem. Manuf. **41**, 599–607 (1998)
39. Ma, Y., Liu, H.P., Zhu, Y.P., et al.: The NARX model-based system identification on nonlinear, rotor-bearing systems. Appl. Sci. **7**, 911 (2017)
40. Hosseini, S.A.A., Khadem, S.E.: Vibration and reliability of a rotating beam with random properties under random excitation. Int. J. Mech. Sci. **49**, 1377–1388 (2007)
41. Luo, Z., Zhu, Y.P., Zhao, X.Y., et al.: Determining dynamic scaling laws of geometrically distorted scaled models of a cantilever plate. J. Eng. Mech. **4**, 04015108 (2016)
42. Hosseini, S.A.A., Khadem, S.E.: Free vibrations analysis of a rotating shaft with nonlinearities in curvature and inertia. Mech. Mach. Theory **44**, 272–288 (2009)
43. Ghafarian, M., Ariaei, A.: Free vibration analysis of a multiple rotating nano-beams system based on the Eringen nonlocal elasticity theory. J. Appl. Phys. **120**, 054301 (2016)
44. Nayfeh, A.H., Pai, P.F.: Linear and Nonlinear Structural Mechanics. Wiley, New York (2004)

45. Dadfarnia, M., Jalili, N., Xian, B., et al.: A Lyapunov-based piezoelectric controller for flexible Cartesian robot manipulators. J. Dyn. Syst. Trans. ASME **126**, 347–358 (2004)
46. Mahmoodi, S.N., Afshari, M., Jahli, N.: Nonlinear vibrations of piezoelectric microcantilevers for biologically-induced surface stress sensing. Commun. Nonlinear Sci. **13**, 1964–1977 (2008)
47. Yang, J.S.: A review of analyses related to vibrations of rotating piezoelectric bodies and gyroscopes. IEEE Trans. Ultrason. Ferroelectr. Freq. Control **52**, 698–706 (2005)
48. Mojahedi, M., Ahmadian, M.T., Firoozbakhsh, K.: The influence of the intermolecular surface forces on the static deflection and pull-in instability of the micro/nano cantilever gyroscopes. Compos. Part B **56**, 336–343 (2014)
49. Ma, H., Wang, D., Tai, X.Y., et al.: Vibration response analysis of blade-disk dovetail structure under blade tip rubbing condition. J. Vib. Control **23**, 252–271 (2017)
50. Sun, Q., Ma, H., Zhu, Y.P., et al.: Comparison of rubbing induced vibration responses using varying-thickness-twisted shell and solid-element blade models. Mech. Syst. Signal Process. **108**, 1–20 (2018)